

Poroelasticity contributes to hydraulic-stimulation induced pressure changes

Nathan Oliver Dutler¹, Benoit Valley¹, Florian Amann², Mohammadreza Jalali³, Linus Villiger⁴, Hannes Krietsch⁵, Valentin Samuel Gischig⁶, Joseph Doetsch⁶, and Domenico Giardini⁷

¹University of Neuchâtel

²RWTH Aachen University

³RWTH Aachen

⁴Swiss Seismological Service

⁵Department of Earth Sciences, ETH Zurich, Switzerland

⁶ETH Zurich

⁷ETH Zürich

November 21, 2022

Abstract

High-pressure fluid injections cause transient pore pressure changes over large distances, which may induce seismicity. The zone of influence for such an injection was studied at high spatial resolutions in six decameter-scaled fluid injection experiments in crystalline rock. Pore pressure time series revealed two distinct responses based on the lag time and magnitude of pressure change, namely, a near- and far-field response. The near-field response is due to pressure diffusion. In the far-field, the fast response time and decay of pressure changes are produced by effective stress changes in the anisotropic stress field. Our experiments prove for the first time that fracture fluid pressure perturbations around the injection point are not limited to the near-field and can extend beyond the pressurized zone.

Hosted file

agusupporting_dutler_poroe.docx available at <https://authorea.com/users/528234/articles/596823-poroelasticity-contributes-to-hydraulic-stimulation-induced-pressure-changes>

1 **Poroelasticity contributes to hydraulic-stimulation induced pressure changes**
2

3 **N.O. Dutler^{1,2}, B. Valley^{1,2}, F. Amann^{1,3}, M. Jalali^{1,3}, L. Villiger^{1,4}, H. Krietsch^{1,5},**
4 **V. Gischig^{1,6}, J. Doetsch^{1,4}, D. Giardini^{1,4}**

5 ¹Swiss Competence Center for Energy Research – Supply of Electricity (SCCER-SoE), ETH
6 Zurich, Switzerland

7 ²Center for Hydrogeology and Geothermics, University of Neuchâtel, Switzerland

8 ³Department of Engineering Geology and Hydrogeology, RWTH Aachen, Germany

9 ⁴Department of Earth Science, ETH Zurich, Switzerland

10 ⁵iLF Beratende Ingenieure AG, Zurich, Switzerland

11 ⁶CSD Ingenieure AG, Bern, Switzerland

12 Corresponding author: Nathan Dutler (nathan.dutler@unine.ch)

13
14 **Key Points:**

- 15 • Pore pressure time series reveal a near-field response dominated by pressure diffusion
16 • The far-field is dominated by a quasi-instantaneous poro-elastic response due to the static
17 anisotropic stress field
18 • Injection data showed pressure changes can extend 3–5 times farther than the pressurized
19 volume because of poroelasticity

20 **Abstract**

21 High-pressure fluid injections cause transient pore pressure changes over large distances, which
22 may induce seismicity. The zone of influence for such an injection was studied at high spatial
23 resolutions in six decameter-scaled fluid injection experiments in crystalline rock. Pore pressure
24 time series revealed two distinct responses based on the lag time and magnitude of pressure
25 change, namely, a near- and far-field response. The near-field response is due to pressure
26 diffusion. In the far-field, the fast response time and decay of pressure changes are produced by
27 effective stress changes in the anisotropic stress field. Our experiments prove for the first time
28 that fracture fluid pressure perturbations around the injection point are not limited to the near-
29 field and can extend beyond the pressurized zone.

30 **Plain Language Summary**

31 The far-field pore pressure response in geological reservoirs due to high pressure fluid injection
32 is not clarified yet. Direct observations of far-field pore pressure changes were analysed in the
33 framework of the In-Situ Stimulation and Circulation project executed at the Grimsel Test Site.
34 The findings show two distinct behaviour, one related to pore pressure diffusion in the near-field
35 of the injection and another one related to poro-elastic effects.

36 **1 Introduction**

37 [1] Hydraulic stimulation operations for enhanced geothermal systems (EGSs), petroleum
38 applications, and wastewater disposal wells are potential sources of seismic hazards. In many
39 places, the high-pressure and/or massive volume of injections has led to an increase in the
40 frequency and magnitude of earthquakes (Bao & Eaton, 2016; Ellsworth, 2013; Frohlich, 2012).
41 Presently, predictions of seismic hazards from injections remain difficult, and determinations of
42 the causality of earthquakes located at a large distance (> 10 km) from injection locations are
43 particularly arduous (Goebel et al., 2017; Keranen et al. 2014).

44 [2] The possible underpinning mechanisms remain under debate. Injection-induced
45 seismicity is frequently explained by the pore pressure increase within the rock mass connected
46 with the injection well. This zone can be referred to as the ‘pressurized zone’, and it can be
47 illuminated by active seismic measurements during high-pressure fluid injections (Calò et al.,
48 2011; Doetsch et al., 2018a; Schopper et al. 2020), as the relative change in p-wave velocity is
49 directly linked to pore pressure changes. These pore pressure changes can lead to fault ruptures,
50 and if the energy at the fracture tip overcomes the tensile strength of the rock, new fractures can
51 be created.

52 [3] Within the pressurized zone, in the near-field of the injection site, the pore pressure
53 distribution is dominated by fluid flow along a pressure gradient, i.e., pressure diffusion.
54 However, the time scale for diffusion-induced pore pressure changes is too slow to explain rapid
55 far-field pressure changes and remotely induced seismic events. One hypothesis explaining
56 remote seismicity is that such activity might be associated with aseismic slip processes. Aseismic
57 slip has been observed in-situ in response to fluid injection (Guglielmi et al., 2015) and can
58 potentially extend beyond the pressurized zone (Bhaattacharya & Cappa, 2015). An alternative
59 hypothesis involves poroelastic processes, which can be used to explain pressure changes caused
60 by rock deformation and associated pore space variations reaching beyond the pressurized zone.
61 This hypothesis has been invoked to describe earthquakes induced more than 30 km away from
62 the injection point (Goebel & Brodsky, 2018).

63 [4] Water level variations in wells related to earthquakes also can be explained by
64 poroelastic effects, and these events offer insights into hydromechanical coupled processes in the
65 crust. The pressure response in wells can range from short oscillation periods in water levels
66 (Cooper et al., 1965) to the recompilation of streamflows, which may subsequently lead to
67 permanent changes in groundwater aquifers and wellhead responses (King et al., 1999;
68 Montgomery & Manga, 2003).

69 [5] In geothermal wells in south Iceland, co- and post-seismic well level changes were
70 observed and correlated with ground motion observations from synthetic aperture radar
71 interferograms (Jónsson et al., 2003). Jónsson et al. (2003) found that poroelastic rebound was
72 dominant following the earthquakes with rapid recovery of the water level. The dependency of
73 the pore pressure on the deviatoric stress component may explain far-field water level
74 fluctuations observed during an earthquake near Parkfield, California (Wang, 1997). While
75 poroelastic effects also can be expected for hydraulic stimulations, these effects have not been
76 observed/analyzed for any subsurface fluid injection projects yet. Mechanical effects (i.e.,
77 poroelastic responses in the far-field) and hydraulic effects (i.e., pressure-diffusion-related
78 responses in the near-field) act on different timescales. Linear poroelastic theory (Biot, 1941) has
79 been developed to predict the mechanical-driven pore pressure changes.

80 **2 Field observations and Methods**

81 **2.1 In-situ Stimulation and Circulation (ISC) project**

82 [6] Here, we present direct in-situ observations of these injection-induced poroelastic
83 effects. In contrast to the aforementioned in-situ poroelastic observations related to deformation
84 induced by large earthquakes, our study presents poroelastic deformation and pressure changes
85 induced by fluid injection. Our study was part of the *In-situ Stimulation and Circulation* (ISC)
86 project (Amann et al., 2018), which was carried out at the Grimsel Test Site (GTS), Switzerland,
87 between 2015 and 2018. The experimental site was located 480 m below surface in the
88 crystalline rock mass of the Aar Massive. The decameter-scale test volume consisted of granitic
89 rocks and a series of brittle to ductile fault zones (Krietsch et al., 2018). The ISC rock mass was
90 accessible through three tunnels from different sides at different elevations.

91 [7] The observations presented here were collected during six hydraulic fracturing
92 experiments (Dutler et al., 2019a). The injection protocol for each experiment consisted of
93 several cycles including (1) breakdown of the formation, (2) two to three refracturing cycles, and
94 (3) a pressure-controlled step-test. The pressure during the injection interval reached a maximum
95 magnitude of 21.2 MPa during the breakdown cycle (injected fluid volume < 2 L). During the
96 subsequent fracture propagation phase, the pressure at the injection point reached values between
97 5.5–9.0 MPa for flow rates up to 90 L/min. In total, volumes of approximately 1000 L per test
98 were injected.

99 [8] Sixty-three packer-isolated intervals in boreholes around the injection locations (Fig.
100 1A) allowed us to capture the 3D fracture fluid pressure response related to six stimulation
101 experiments. The Euclidian distance r from the midpoint of the injection point to the midpoints
102 of the pressure monitoring interval ranged from a few meters up to 100 m. Most of the pore
103 pressure intervals in the far-field were above the injection location, with an elevation difference
104 of 10–40 m. After each experiment, a depressurization phase was carried out by venting the

105 packer intervals within the pressurized zone. Up to 12 hours were required to recover the initial
106 pore pressure levels.

107 2.2 Methods

108 [9] The presented analysis is based on the hydraulic fracturing (Dutler et al., 2019a) and
109 hydraulic shearing (Krietsch et al., 2020a) public datasets Dutler et al. (2019b) and Krietsch et al.
110 (2019b). For this analysis we used pressure and strain observations. The ISC monitoring setup
111 and the description is published (Doetsch et al., 2018b).

112 [10] The geological model incl. borehole logs and visualization is available (Krietsch et
113 al., 2018a) as public dataset (Krietsch et al., 2018b). The far-field pore pressure was sampled all
114 60 s during the HF experiments. The Data S1 includes the location of the borehole and the
115 borehole intervals. For this the geological model visualization was updated with the additional
116 boreholes and intervals and can be inquired by the corresponding author.

117 [11] The timeseries were filtered with a lowpass second order Butterworth filter for
118 picking. The timeseries were cut into the refrac cycles (RF1, RF2 and RF3 in Fig. S1). The
119 highlighted section in the picking plots indicates fluid injection. The shut-in time t_s is defined as
120 the time, when fluid injection is stopped followed by an observation phase, which ends either
121 with a new injection cycle or the depressurization of the system, opening the ISC injection and
122 pore pressure observation intervals. The characteristic time t_c is the difference between the
123 picking time t_{pick} and shut-in time t_s . For the pore pressure and strain observations, the time was
124 picked due to reaching a minimum, maximum or a notable change in magnitude during the
125 observation phase (Fig. S1). For the pore pressure timeseries we used in general the latter pick
126 with bigger absolute magnitude, which is hydraulically driven. For the uniaxial strain timeseries,
127 the earliest pick was used as it is an indication of mechanical driven one. All results can be found
128 in Data S2 (pore pressure), Data S4 (strain).

129 [12] For each HF experiment the absolute maximum magnitudes were picked from the
130 pore pressure timeseries during the two refrac cycles RF1 and RF2. These two cycles correspond
131 to the biggest fluid volume without depressurization and highest flow rates. The corresponding
132 injected volume was calculated for the time corresponding to the absolute maximum magnitude.
133 Both results can be found in Data S3 and both are visualized (see Fig. 2B, S4A and S5B).

134 [13] Outside of the pressurized zone, we assume that the change in pore pressure is linked
135 with the mean stress change $\sigma_m = \frac{1}{3}(\Delta\sigma_{11} + \Delta\sigma_{22} + \Delta\sigma_{33})$ and the Biot-Willis coefficient α .
136 Volumetric strain is then calculated from the mean stress change and the known Young's
137 modulus K for the rock mass. Then,

$$\Delta p = \alpha \sigma_m$$

$$\sigma_m = K \epsilon_{vol}$$

138 where α is between 0.64 and 0.71 and $K = 19$ GPa (Selvadurai, Selvadurai & Nejati,
139 2019).

140 [14] Extract from Detournay & Cheng (1988) presenting the pore-pressure solution
141 induced by the pressurization of an infinite vertical cylinder. The three fundamental modes to
142 solve the problem are (i) the far-field isotropic stress, (ii) the in-situ pore pressure and (iii) the
143 far-field stress deviator.

144 • Mode 1

145 The mode 1 corresponds to the classical Lamé solution and does not include a pore
146 pressure term.

147 • Mode 2

148 The pore pressure field is solved for an uncoupled homogeneous diffusion equation
149 taking the Laplace transform (with inversion parameter s). For the boundary conditions in the
150 far-field the in-situ pore pressure, p_0 , is reached and the stress component vanish. The pore
151 pressure field is solved using by the Laplace transformed solution (Eq. 23, Detournay & Cheng,
152 1988):

$$\frac{s\tilde{p}^{(2)}}{p_0} = -\frac{K_0(\xi)}{K_0(\beta)}$$

153 where K_0 is the modified Bessel function of second kind of order zero, $\xi = r\sqrt{s/D}$ and
154 $\beta = a\sqrt{s/D}$. The parameters a and D are cylinder radius, and the diffusivity coefficient. The
155 radius r indicates the distance between the cylinder radius and a given observation point.

156 • Mode 3

157 For a deviatoric stress field the pore pressure solution is also given in the Laplace
158 transform domain. The solution reads:

159

$$\frac{s\tilde{p}^{(3)}}{S_0 \cos 2\theta} = \frac{B^2(1-\nu)(1+\nu_u)^2}{9(1-\nu_u)(\nu_u-\nu)} C_1 K_2(\xi) + \frac{B(1+\nu_u)}{3(1-\nu_u)} C_2 \frac{a^2}{r^2}$$

160

$$C_1 = -\frac{12\beta(1-\nu_u)(\nu_u-\nu)}{B(1+\nu_u)(D_2-D_1)}$$

161

$$C_2 = \frac{4(1-\nu_u)D_2}{D_2-D_1}$$

162

$$D_1 = 2(\nu_u-\nu)K_1(\beta)$$

163

$$D_2 = \beta(1-\nu)K_2(\beta)$$

164

165 where K_n is the modified Bessel function of second kind of order n . The parameters, S_0 ,
166 B , ν_u , ν are stress deviator, Skempton coefficient, undrained and drained Poisson's ratio. The
167 $\cos 2\theta$ on the lhs indicate that the problem is not axisymmetric. The first term on the rhs depends
168 only on the modified Bessel function of order 2 all the other parameters are constant. The second
169 term on the rhs depends on r^{-2} and is the mechanical component, which drives the magnitude

170 decay in the far-field. The instantaneous drilling of the cylinder generates the following
 171 approximation for the undrained pore pressure distribution given by Eq. 50 (Detournay & Cheng,
 172 1988):

$$p^0 = \frac{4}{3} S_0 B (1 + \nu_u) \frac{a_c^2}{r^2} \cos 2\theta$$

173 [15] In the following we describe the fitting process, to achieve the “poroelastic solution”
 174 presented in Fig. 2B, S4A and S5B. Two fitting parameters are introduced with a corresponding
 175 cylinder radius, a_c and a corresponding injection time, t_d . The parameters for the pore pressure
 176 solution can be found in Table 1.

177 [16] The late time approximation $p(r, \theta)$ and p^0 are equated, where the values p_a and a
 178 for the envelope $p(r, \theta)$ are given. The two terms equated and solved for a_c to achieve the new
 179 corresponding cylinder radius. The mean stress p_0 is estimated from the six injection
 180 experiments during the refracturing cycles and the deviatoric component S_0 is the difference of
 181 the minimum and maximum principal stress magnitude divided by 2. The diffusivity coefficient
 182 is estimated from the pressurized near-field zone presented in Fig. 2A. The other values are from
 183 the literature or calculated from the values given in Table 1.

184 [17] The first fitting parameter gives a value a_c equal to 2.80 m allow us to match the
 185 elastic approximation with the far-field observations decaying with a rate r^{-2} . Nevertheless, we
 186 use a value of 2.60 m for pore pressure solution obtained by the numerical Laplace inversion
 187 model, due to inaccuracies due to the transformation. The numerical results in the time domain
 188 are obtained using a numerical Laplace inversion model of Stehfest (1970).

189 [18] Fig. S3A and S3B present the solutions for Mode 2 and Mode 3 for various times t_d ,
 190 which corresponds to possible injection times. The pore pressure solution is then presented by
 191 the superposition of $p^{(2)} + p^{(3)}$ in Fig. S3C. The injection time in our case is around 1200 s.
 192 Indeed, the solution for t_d equal to 1200 s is able to build an envelope to the observations, which
 193 is a good match between the model and our observations.

194 The Skempton coefficient is given by (Wang, 2000):

$$B = \frac{3(\nu_u - \nu)}{\alpha(1 - 2\nu)(1 + \nu_u)}$$

195 **3 Spatial and time effect on pore pressure response**

196 [19] Examples of pressure data are presented in Fig. 1B. All of the pressure records were
 197 classified based on their pressure response during the experiments as being positive (pressure
 198 increase), negative (pressure decrease), or mixed (pressure increase and decrease from one
 199 experiment to the next). In addition, for each monitoring point, the perturbation magnitude was
 200 extracted. The perturbation magnitude is defined as the extremum (negative or positive) pressure
 201 perturbation magnitude observed during each experiment. The characteristic time was estimated
 202 by the elapsed time between the maximum pressure in the injection interval (which is normally
 203 the shut-in time) and pressure perturbation extremum in the observation intervals (Fig. S1).

204 [20] In total, we observed 28 positive, 28 negatives, and 7 mixed responses (Fig. 1C).
 205 Far-field monitoring intervals tended to always present the same response, while mixed
 206 responses were more common in the near-field. In the near-field (up to 30 m), the pressure

207 response was dominantly positive (Fig. 1A), although mixed and negative responses also were
208 present.

209 [21] Negative pore pressure responses due to the stress/strain redistribution were driven
210 by the fluid injection into the fractured rock mass. Positive responses were primarily associated
211 with a hydraulic connection to the injection point, and these also may have been related to
212 fracture closure and volumetric compression. The near-field zone dominated by positive and
213 mixed responses is referred to as the pressurized zone. An example of a mixed response is given
214 by the PRP11 interval presented in Fig. 1B, which showed a positive response (HF1–HF5, red)
215 except during HF6 when a negative response was observed (blue in Fig. 1B). These exceptions
216 were induced by local heterogeneities in the structure and flow, and such data can be explained
217 only when the small-scale heterogeneities and their configuration with respect to the injection
218 point are considered (Dutler et al., 2021).

219 [22] The pore pressure intervals in the far-field were consistently negative or positive for
220 all experiments, i.e., there were no mixed responses, except for during experiment HF5. This can
221 be explained by the peculiar flow situation during this test because a short-cut was created to an
222 open borehole during the first refracturing cycle and the far-field pressure perturbation during
223 this test was below our detection threshold. The spatial repartition of positive and negative
224 responses was not random, and entire zones seemed to consistently present a positive or negative
225 response.

226 [23] The analyses of the characteristic time showed a distinct pattern for the two zones
227 (Fig. 2A), i.e., longer characteristic times in the near-field zone related to fluid pressure
228 diffusion, and shorter characteristic times in the far-field zone dominated by a mechanical
229 response. We will refer to the fracture fluid pressure for the near-field zone with a dominant fluid
230 diffusion component. In the far-field, we will refer to the pore pressure while assuming that the
231 fractured medium can be described equivalently with the poroelasticity.

232 [24] The pressurized near-field zone had diffusivity coefficients ranging from 0.01 to 1
233 m^2/s , as estimated by assuming normal radial diffusion in 2D, and these data are indicated by the
234 gray dashed lines in Fig. 2A. The broad range of coefficients indicates that pressure propagation
235 was not dominated by simple linear diffusion. Pressure propagation occurred in an
236 interconnected fracture network with a hierarchical organization of flow from main channels
237 initiating at the injection point and branching to subsidiary channels further away from the
238 injection point. This geometry expanded during continuous stimulation operations (Dutler et al.,
239 2020). Ultimately, this led to a very heterogeneous flow field with a large contrast of flow
240 velocities as reflected by the broad range of equivalent diffusivity coefficients observed.

241 [25] Based on our characteristic time analyses, this near-field zone extended up to about
242 30 m for our experiments (Fig. 2A). This size is comparable with the extent of the pressurized
243 zone estimated by Schopper et al. (2020) based on seismic time-lapse tomography. The zone,
244 where we observed seismic signals, was significantly smaller with an extent of 20 m as indicated
245 by the dashed green line of Fig. 2A (Dutler et al., 2019a; Villiger et al., 2020).

246 [26] In addition, 60 uniaxial strain gauges captured the strain response in this zone, and
247 the data were indicative of complex hydromechanical interactions (Fig. S2). The strain signals
248 exhibited very rapid responses that can be explained either by poroelastic effects or by focused
249 flow channeling. Both processes were likely active simultaneously as supported by the

250 observations of some rapid pressure perturbations in the near-field that provided evidence for
251 focused flow in deformed fractures (Fig. S5).

252 [27] Far-field data formed a distinct group with a faster characteristic response time
253 leading to increased velocities. These velocities presented with equivalent diffusivity coefficients
254 ranging from 1 to 100 m²/s (Fig. 2A). These values are unrealistically high for a diffusive
255 process. The 1/60 Hz sampling rate used to capture the far-field pore pressure responses posed
256 limitations for estimating the maximal diffusivity coefficient. As already discussed, the far-field
257 responses were both positive and negative. The near-instantaneous pore pressure response in the
258 far-field zone was suggestive of strong mechanical coupling.

259 [28] The analyses of the pressure perturbation magnitude (Fig. 2B) confirmed the
260 presence of the two different processes. The pressure perturbation was largest at the injection
261 point and in its vicinity. In the far-field, pressure perturbations were visible up to 100 m away
262 from the injection location, although the maximum pore pressure change at that distance was
263 only ~3 kPa. So, the ratio between the size of the pressurized zone (radius of 20–30 m) and the
264 farthest perturbation reach was at least on the order of 3 to 5. The maximum or minimum pore
265 pressures were generally observed during the injection phases with the highest flow rates (Fig.
266 1B).

267 [29] The largest observed pressure perturbations in the near-field up to a distance of 30 m
268 did not exceed the pressure predicted by a radial pressure diffusion model with a diffusivity of
269 0.1 m²/s, a test time of 600 s, and the actual imposed pressure at the injection point (Fig. 2B).
270 Beyond 30 m, however, such a model predicted a pressure perturbation magnitude that was at
271 least an order of magnitude below the largest observed perturbation. In addition, between 40 and
272 60 m, we mainly observed negative pressure responses, which cannot be explained by pressure
273 diffusion.

274 **4 Importance of static deviatoric stress field component**

275 [30] Detournay and Cheng (1988) presented a solution for the pore pressure induced by
276 the pressurization of a vertical cylinder with two principal stress components parallel to the
277 cylinder axis. The cylinder axis is of infinite length. The physical interpretation of this problem
278 can be decomposed into the following three fundamental loading modes: (i) the far-field
279 isotropic stress, (ii) the in-situ pore pressure, and (iii) the far-field stress deviator. Each mode has
280 to be solved, and the superposition of all three modes leads to the solution (Fig. S3). The far-field
281 approximation (iii) of the pore pressure is asymmetric and dependent on a magnitude decay on
282 the order of r^{-2} . A simplified approximation is presented for the volumetric pore pressure
283 changes p :

$$p(r, \theta) = p_a \frac{a^2}{r^2} \cos(2\theta),$$

284 where a given uniform radial stress $p_a = 400$ kPa and cylinder radius $a = 10$ m with the
285 directional angle $\theta = 0$ corresponds to the upper envelope for the far-field distance in Fig. 2B.
286 Mode (iii) has a far-field stress deviator leading to a positive and negative pore pressure response
287 depending on the orientation, which is related to the directional angle. The zone between 30 and
288 50 m represents a transition zone between the pressurized zone dominated by pressure diffusion
289 in the near-field and volumetric pore deformation in the far-field.

290 [31] A similar approach was used for modeling pressure around fluid disposal wells in
291 Oklahoma, where the fluid disposal wells were located approximately 40 km away from the
292 earthquake epicenter (Goebel et al., 2014). However, the decoupling of elasticity and diffusion
293 has its limitations because positive and negative pore pressure responses remain unexplained. To
294 explain the observed spectrum of pressure responses, a solution with deviatoric stress boundary
295 conditions is required. The poroelastic solution for a cylinder given by Detournay and Cheng
296 (1988) inherently contains this effect and can explain changes of criticality on faults in the far-
297 field of a stimulation. The applied poroelastic solution was fitted by independent values, i.e., the
298 corresponding cylinder radius and injection time. This allowed us to achieve a good match for
299 the observations and the poroelastic solution presented in Fig. 2B (and Fig. S4A and S5B). Fluid
300 flow during the experiments was limited to interconnected fractures. In the far-field zone,
301 pressure changes were assumed to be independent of active fluid transport from the pressurized
302 zone, which agreed well with the presented poroelastic solution.

303 [32] The pore pressure solution is presented for the diffusion (ii) and deviatoric (iii)
304 components separately (Fig. 3). The diffusion component of the pore pressure solution
305 dominated up to 42 m from the injection location. The radial pressurization was a strong
306 simplification. Two fault zone sets S1 and S3 were striking through the targeted volume. The S3
307 structures were in the brittle-ductile fault zone (Fig. 3C) containing two-fracture systems
308 (Krietsch et al., 2018). One was striking parallel to the S3 fault zone, and the other was abutting
309 at high angles to the fault zone. The second set of ductile fault zones (S1, Fig. 3D) was
310 associated with a single fracture system striking parallel to the fault zones. It is more likely that
311 the injections created an ellipsoidal shaped pressurized zone along the S3 faults due to the (1)
312 stress field, (2) fracture connectivity (3), and fracture orientation. These interconnected,
313 permeable fractures would allow for the transportation of fluids over larger distances, but are not
314 necessarily the most critical structures for failures depending on the stress regime. The
315 ellipsoidal shape caused compression normal to the S3/S1 fault zones and negative pore pressure
316 responses at the ellipsoidal tip (Fig. 3C and 3D). Compared to the deviatoric solution, which
317 dominated the far-field response, the ellipsoid only explained the observed negative responses in
318 front of the ellipsoidal tip occurring in front of the pressurized zone.

319 [33] Pore pressure responses in the far-field were the largest in magnitude for the tests
320 (HF1, HF2, and HF6) located next to the S1 structure (Fig. 1A) and reached to only part of the
321 magnitude for tests next to the S3 structure. The deviatoric pore pressure component (Fig. 3B)
322 was not radially symmetric due to the deviatoric stress field component (Fig. 3E), which is given
323 in the lower stereographic projection for the presented solution on a vertical cylinder. The six
324 hydraulic fracturing experiments allowed us (Dutler et al., 2020; Krietsch et al., 2019a) to
325 specify the stress state toward the direction north of the S3 structure, which is presented in the
326 lower stereographic projection (Fig. 3E). The orientation of the minimum and maximum
327 principal stress component was used (S_1 and S_3) for the rotation of the deviatoric component.
328 This led to far-field pore deformation with a characteristic positive/negative response, which was
329 dominant outside of the cylinder (Fig. 3E). The observations agreed frequently with the
330 presented solution outside of the cylinder. A few exceptions existed around the tunnels, and these
331 were probably influenced by secondary effects like (1) the stress field and (2) the drained rock
332 mass.

333 **5 Conclusions**

334 [34] Our observations prove for the first time experimentally, that fracture fluid pressure
335 perturbations around the injection point are not limited to the near-field, which is affected by
336 diffusion processes. Importantly, our data show that pressure in the far-field is associated with
337 pore volume changes. The observations indicate that an already small hydraulic power (flow rate
338 times injection pressure) can cause a far-field poroelastic pressure response. The spatial
339 distribution of negative and positive responses can provide important information about the
340 dominant failure mechanism before any hazardous seismicity occurs. The spatially sparse
341 information from the poroelastic response has the advantage that it can overcome the spatial
342 resolution constraint of the seismic network. Thus, this can serve as a complementary method for
343 seismic monitoring during hydraulic stimulations. With appropriate considerations, this
344 technique could be used to develop mitigation strategies for seismic hazards, particularly if wells
345 surrounding an injection site are equipped with packers and pressure gauges. In summary, the
346 proposed method could represent a powerful and cost-effective monitoring tool.

347 **Acknowledgments, Samples, and Data**

348 Acknowledgments: This study was part of the In-situ Stimulation and Circulation (ISC)
349 project established by the Swiss Competence Center for Energy Research-Supply of Electricity
350 (SCCER-SoE) with the support of Innosuisse. The Grimsel Test Site is operated by Nagra, the
351 National Cooperative for the Disposal of Radioactive Waste. We are indebted to Nagra for
352 hosting the ISC experiment in their GTS facility and to the Nagra technical staff for on-site
353 support and allowing us to publish the dataset of the far-field pressure response. We thank Bill
354 Lanyon for the data compilation of the far-field pressure response.

355 Funding: Funding for the ISC project was provided by the ETH Foundation with grants
356 from Shell and EWZ and by the Swiss Federal Office of Energy through a P&D grant. This
357 research was supported by the Swiss National Foundation (Grant nos. 200021-165677 (Nathan
358 Dutler), 200021-169178 (Hannes Krietsch)) and the Federal Institute of Technology Zurich
359 (Grant no. ETH-35-16-1 (Linus Villiger)).

360 Author Contributions: The monitoring setup was designed by VG, JD, LV, HK, MRJ,
361 and FA. The injection protocol for the HF experiments was designed by NOD and BV. All of the
362 authors were part of the data acquisition team during the experiments of the ISC project; FA was
363 the project administrator. The data curation, formal analysis, investigation, and data
364 visualization, including writing the original draft, were done by NOD with the help of BV and
365 FA. The writing, review, and editing were done by MRJ, LV, HK, VG, and JD.

366 Competing Interests: The authors declare no competing interests.

367 Data and Materials Availability: All of the material for the analysis is available in the
368 supplementary material. The raw data are available under an open access license for non-
369 commercial use and are accessible via the ETH research collection at
370 <https://doi.org/10.3929/ethz-b-000328270> (Dutler et al., 2019b), <https://doi.org/10.3929/ethz-b-000328266> (Krietsch et al., 2019b), and <https://doi.org/10.3929/ethz-b-000243199> (Krietsch et
371 al., 2018b).
372
373

374 **References**

- 375 F. Amann, V. Gischig, K. Evans, J. Doetsch, R. Jalali, B. Valley, H. Krietsch, N. Dutler, L.
376 Villiger, B. Brixel, M. Klepikova, A. Kittilä, C. Madonna, S. Wiemer, M. O. Saar, S.
377 Loew, T. Driesner, H. Maurer, D. Giardini, The seismo-hydromechanical behavior during
378 deep geothermal reservoir stimulations: open questions tackled in a decameter-scale in
379 situ stimulation experiment. *Solid Earth* 9(1), 115–137 (2018). [https://doi.org/10.5194/se-](https://doi.org/10.5194/se-9-115-2018)
380 9-115-2018
- 381 X. Bao, D. W. Eaton, Fault activation by hydraulic fracturing in western Canada. *Science*
382 354(6318), 1406–1409 (2016). <https://doi.org/10.1126/science.aag2583>
- 383 P. Bhattacharya, R. C. Viesca, Fluid-induced aseismic fault slip outpaces pore-fluid migration.
384 *Science* 364(6439), 464–468 (2019). <https://doi.org/10.1126/science.aaw7354>
- 385 M. A. Biot, General theory of three-dimensional consolidation. *Journal of Applied Physics* 12,
386 155 (1941). <https://doi.org/10.1063/1.1712886>
- 387 M. Calò, C. Dorbath, F. H. Cornet, N. Cuenot, Large-scale aseismic motion identified through 4-
388 D P-wave tomography. *Geophysical Journal International* 186(3), 1295–1314 (2011).
389 <https://doi.org/10.1111/j.1365-246X.2011.05108.x>
- 390 H. Cooper, J. Bredehoeft, I. Papadopoulos, R. Bennett, The Response of Well-Aquifer Systems to
391 Seismic Waves. *Journal of Geophysical Research* 70(16), 3915–3926 (1965).
- 392 M. L. T. Dambly, M. Nejati, D. Vogler, M. O. Saar, On the direct measurement of shear moduli
393 in transversely isotropic rocks using the uniaxial compression test. *Int. J. Rock Mech.*
394 *Min. Sci.* 113, 220–240 (2019).
- 395 E. Detournay, A. H.-D. Cheng, Poroelastic response of a borehole in a non-hydrostatic stress
396 field. *International Journal of Rock Mechanics and Mining Sciences & Geomechanics*
397 *Abstracts* 25(3), 171–182 (1988). [https://doi.org/10.1016/0148-9062\(88\)92299-1](https://doi.org/10.1016/0148-9062(88)92299-1)
- 398 J. Doetsch, V. S. Gischig, L. Villiger, H. Krietsch, M. Nejati, F. Amann, M. Jalali, C. Madonna,
399 H. Maurer, S. Wiemer, T. Driesner, D. Giardini, Subsurface Fluid Pressure and Rock
400 Deformation Monitoring Using Seismic Velocity Observations. *Geophysical Research*
401 *Letters* 45(19), 10389–10397 (2018a). <https://doi.org/10.1029/2018GL079009>
- 402 J. Doetsch, V. Gischig, H. Krietsch, L. Villiger, F. Amann, N. Dutler, M. Jalali, B. Brixel, C.
403 Roques, P.L. Giertzuch, A. Kittilä, R. Hochreutener, “Grimsel ISC Experiment
404 Description” (Tech. Rep. Zurich, 2018b). <https://doi.org/10.3929/ethz-b-000310581>
- 405 N. O. Dutler, B. Valley, V. Gischig, L. Villiger, H. Krietsch, J. Doetsch, B. Brixel, M. Jalali, F.
406 Amann, Hydraulic fracture propagation in a heterogeneous stress field in a crystalline
407 rock mass. *Solid Earth* 10(6), 1877–1904 (2019a). [https://doi.org/10.5194/se-10-1877-](https://doi.org/10.5194/se-10-1877-2019)
408 2019
- 409 N. O. Dutler, V. Gischig, J. Doetsch, M. Jalali, H. Krietsch, F. Amann, Hydro mechanical data
410 set from the six Grimsel ISC hydraulic fracturing experiments, (2019b).
411 <https://doi.org/10.3929/ethz-b-000328270>
- 412 N. O. Dutler, B. Valley, V. S. Gischig, M. Jalali, B. Brixel, H. Krietsch, C. Roques, F. Amann,
413 Hydromechanical insight of fracture opening and closure during in-situ hydraulic

- 414 fracturing in crystalline rock. *Int. J. Rock Mech. Min. Sci.* 135(10), 104450 (2020).
415 <https://doi.org/10.1016/j.ijrmms.2020.104450>
- 416 N. O. Dutler, B. Valley, L. Villiger, V. Gischig, F. Amann, Observation of a repeated step-wise
417 fracture growth during hydraulic fracturing experiment at the Grimsel Test Site. In
418 *Proceedings World Geothermal Conference, Reykjavik, 21–26 May 2021.*
- 419 W. L. Ellsworth, Injection-Induced Earthquakes. *Science* 341(6142), 1225942–1225942 (2013).
420 <https://doi.org/10.1126/science.1225942>
- 421 C. Frohlich, Two-year survey comparing earthquake activity and injection-well locations in the
422 Barnett Shale, Texas. *Proceedings of the National Academy of Sciences of the United*
423 *States of America* 109(35), 13934–13938 (2012).
424 <https://doi.org/10.1073/pnas.1207728109>
- 425 T. H. W. Goebel, M. Weingarten, X. Chen, J. Haffener, E. E. Brodsky, The 2016 Mw5.1
426 Fairview, Oklahoma earthquakes: Evidence for long-range poroelastic triggering at >40
427 km from fluid disposal wells. *Earth and Planetary Science Letters* 472, 50–61 (2017).
428 <https://doi.org/10.1016/j.epsl.2017.05.011>
- 429 T. H. W. Goebel, E. E. Brodsky, The spatial footprint of injection wells in a global compilation
430 of induced earthquake sequences. *Science* 361(6405), 899–904 (2018).
431 <https://doi.org/10.1126/science.aat5449>
- 432 Y. Guglielmi, F. Cappa, J.-P. Avouac, P. Henry, D. Elsworth, Seismicity triggered by fluid
433 injection – induced aseismic slip. *Science* 348(6240), 1224–1227 (2015).
434 <https://doi.org/10.1126/science.aab0476>
- 435 S. Jónsson, P. Segall, R. Pedersen, G. Björnsson, Post-earthquake ground movements correlated
436 to pore-pressure transients. *Nature* 424(6945), 179–183 (2003).
437 <https://doi.org/10.1038/nature01776>
- 438 K. M. Keranen, M. Weingarten, G. A. Abers, B. A. Bekins, S. Ge, Sharp increase in central
439 Oklahoma seismicity since 2008 induced by massive wastewater injection. *Science*
440 345(6195), 448–451 (2014). <https://doi.org/10.1126/science.1255802>
- 441 C.-Y. King, S. Azuma, G. Igarashi, M. Ohno, H. Saito, H. Wakita, Earthquake-related water-
442 level changes at 16 closely clustered wells in Tono, central Japan. *Journal of Geophysical*
443 *Research: Solid Earth* 104(B6), 13073–13082 (1999).
444 <https://doi.org/10.1029/1999JB900080>
- 445 H. Krietsch, J. Doetsch, N. Dutler, M. Jalali, V. Gischig, S. Loew, F. Amann, Comprehensive
446 geological dataset describing a crystalline rock mass for hydraulic stimulation
447 experiments. *Scientific Data* 5, 180269 (2018a). <https://doi.org/10.1038/sdata.2018.269>
- 448 H. Krietsch, J. Doetsch, N. Dutler, M. Jalali, V. Gischig, S. Loew, F. Amann, Comprehensive
449 geological dataset for a fractured crystalline rock volume at the Grimsel Test Site,
450 (2018b). <https://doi.org/10.3929/ethz-b-000243199>
- 451 H. Krietsch, V. Gischig, K. Evans, J. Doetsch, N. O. Dutler, B. Valley, F. Amann, Stress
452 Measurements for an In Situ Stimulation Experiment in Crystalline Rock: Integration of
453 Induced Seismicity, Stress Relief and Hydraulic Methods. *Rock Mechanics and Rock*
454 *Engineering* 52(2), 517–542 (2019a). <https://doi.org/10.1007/s00603-018-1597-8>

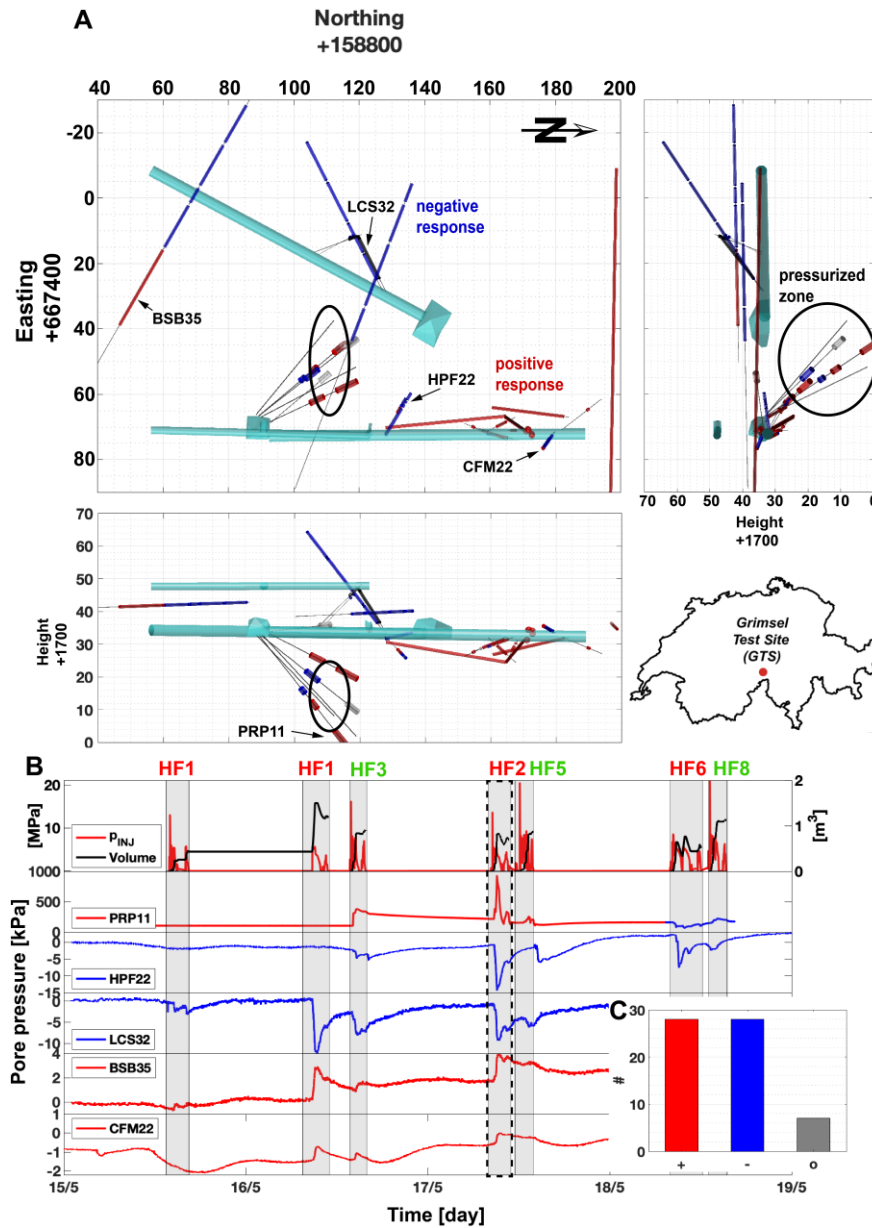
- 455 H. Krietsch, V. Gischig, J. Doetsch, M. Jalali, F. Amann, Hydro mechanical data set from the six
456 Grimsel ISC hydraulic shearing experiments, (2019b). [https://doi.org/10.3929/ethz-b-](https://doi.org/10.3929/ethz-b-000328266)
457 000328266
- 458 H. Krietsch, V. S. Gischig, J. Doetsch, K. F. Evans, L. Villiger, M. Jalali, B. Valley, S. Loew, F.
459 Amann, Hydro-mechanical processes and their influence on the stimulation effected
460 volume: Observations from a decameter-scale hydraulic stimulation project. *Solid Earth*
461 *Discuss.*, (2020). <https://doi.org/10.5194/se-2019-204>
- 462 D. R. Montgomery, M. Manga, Streamflow and water well responses to earthquakes. *Science*
463 300(5628), 2047–2049 (2003). <https://doi.org/10.1126/science.1082980>
- 464 F. Schopper, J. Doetsch, L. Villiger, H. Krietsch, V. S. Gischig, M. Jalali, F. Amann, N. Dutler,
465 H. Maurer, On the Variability of Pressure Propagation during Hydraulic Stimulation
466 based on Seismic Velocity Observations. *Journal of Geophysical Research: Solid Earth*
467 125, e2019JB018801 (2020). <https://doi.org/10.1029/2019JB018801>
- 468 P. Selvadurai, P. A. Selvadurai, M. Nejati, A multi-phasic approach for estimating the Biot
469 coefficient for Grimsel granite. *Solid Earth* 10, 2001–2014 (2019).
- 470 H. Stehfest, Algorithm 368: Numerical inversion of Laplace transforms [D5]. *Commun. ACM*
471 13, (1970). doi:10.1145/361953.361969
- 472 L. Villiger, V. S. Gischig, J. Doetsch, H. Krietsch, N. O. Dutler, M. Jalali, B. Valley, P. A.
473 Selvadurai, A. Mignan, K. Plenkens, D. Giardini, F. Amann, S. Wiemer, Influence of
474 reservoir geology on seismic response during decameter-scale hydraulic stimulations in
475 crystalline rock. *Solid Earth* 11(2), 627–655 (2020). [https://doi.org/10.5194/se-11-627-](https://doi.org/10.5194/se-11-627-2020)
476 2020
- 477 H. F. Wang, Effects of deviatoric stress on undrained pore pressure response to fault slip. *Journal*
478 *of Geophysical Research* 102(97), 17943–17950 (1997).
- 479 H. Wang, *Theory of Linear Poroelasticity with Applications to Geomechanics and Hydrogeology*
480 (Princeton University Press, 2000).

481

482

483

484

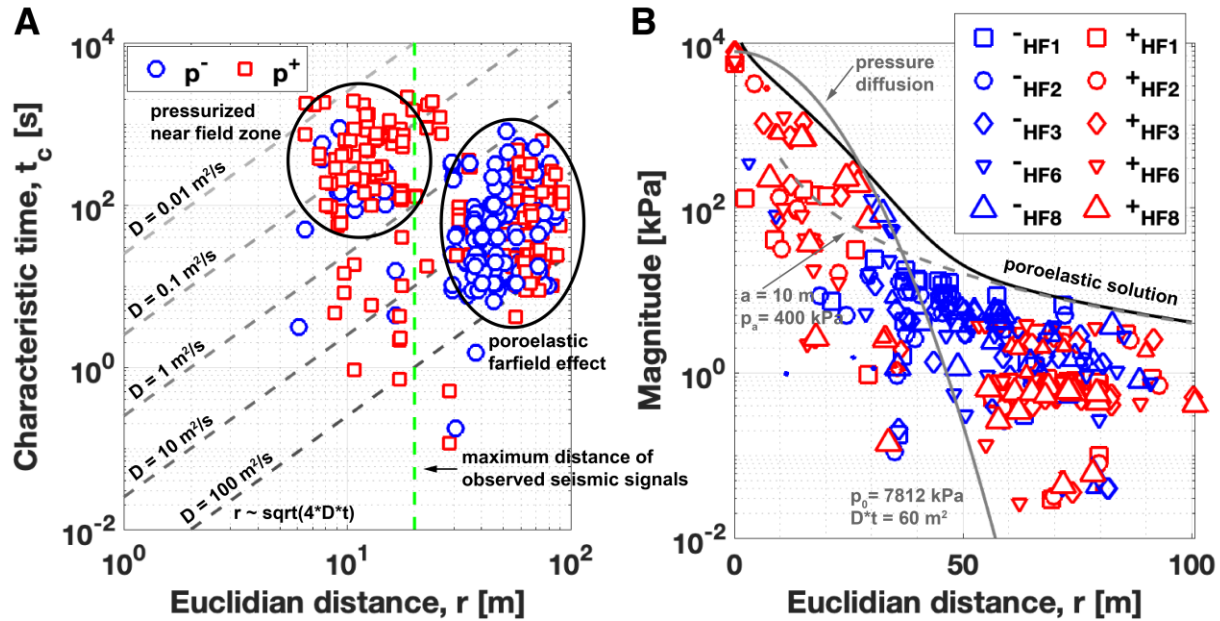


485

486 **Fig. 1. Time series of the pore pressure observations were classified by positive or negative**
 487 **responses.** (A) The interval locations are indicated and labeled in the plane and profile view, and
 488 data show the positive (red), negative (blue), and mixed (gray) magnitude response in the open
 489 intervals including the approximate pressurized zone and access tunnels. Coordinates on panel
 490 (A) are referenced to the Swiss metric coordinate system (CH1903+). (B) Time series of the
 491 injection pressure (red solid) and volume (black solid), where PRP11 is the open interval
 492 pressure in the pressurized zone and the other four are open intervals indicative of the far-field
 493 response. The location of the intervals is indicated in (A). (C) Proportion of positive, negative,
 494 and mixed responses.

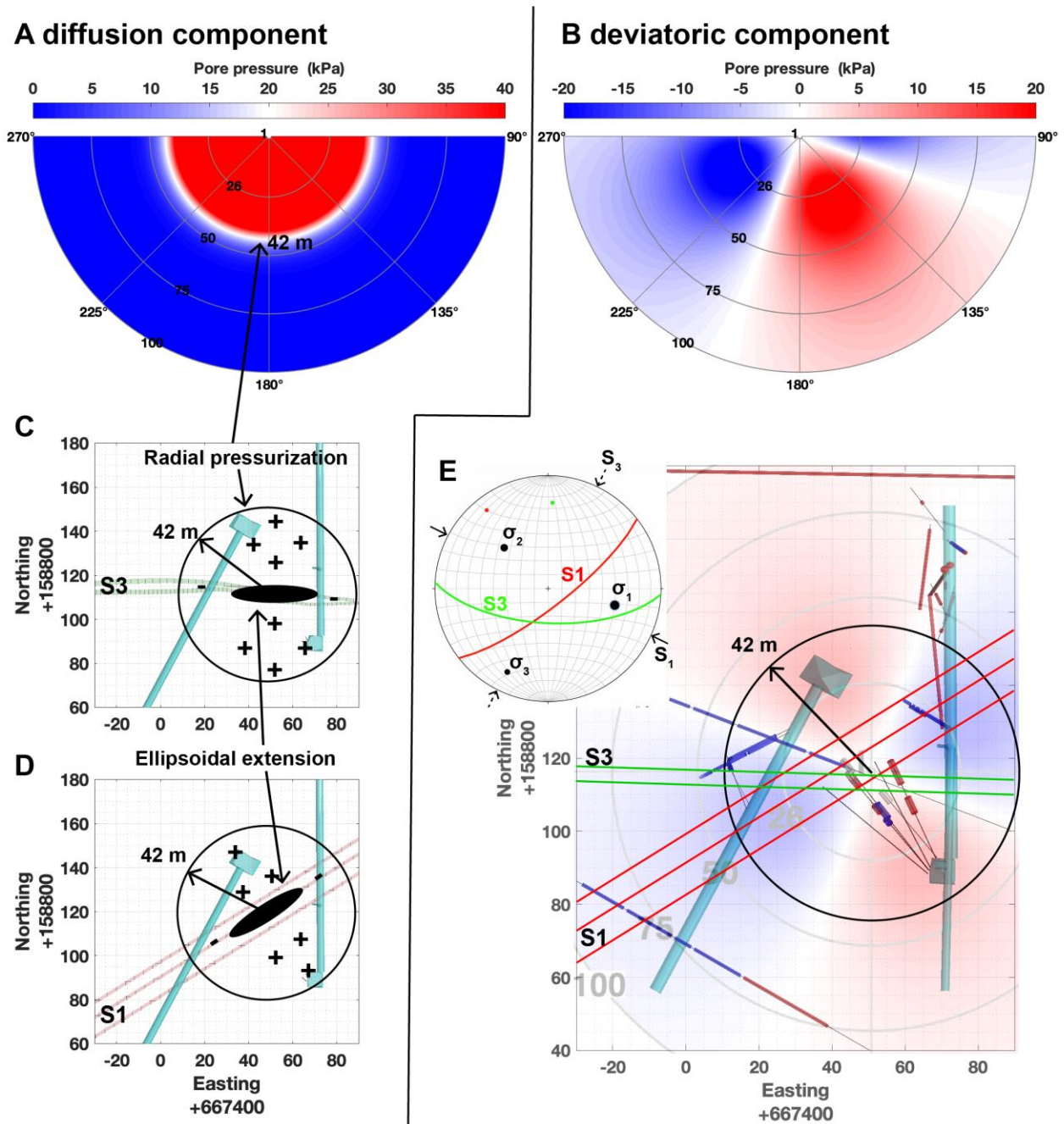
495

496



497

498 **Fig. 2. Spatial time increase and spatial maximum absolute pressure magnitude were**
 499 **classified as positive (red) and negative (blue).** (A) The log–log plot presents the characteristic
 500 time t_c against the Euclidian distance r along with gray dashed lines that indicate the different
 501 diffusivity coefficients for the 1D diffusion equation. Two different patches were observed for
 502 the pressure observations, one corresponding to the pressurized near-field zone and the other to
 503 the poroelastic far-field response. The green dashed line indicates the maximum distance of
 504 observed seismic signals. (B) The maximum magnitude is presented, including the volume
 505 dependent size of the symbols against the Euclidian distance r for specific tests on a semi-log
 506 scale (see Fig. S4A for the log–log scale). The poroelastic solution (black solid line), radial
 507 pressure diffusion (gray solid line), and far-field pore pressure solution are drawn (gray dashed
 508 line).
 509



510

511 **Fig. 3. Pore pressure response as interpreted by the diffusion and deviatoric component.**
 512 (A) The pressurized radial-symmetric solution for a cylinder dominated up to 42 m with a
 513 magnitude of 20 kPa. (B) The deviatoric component started to dominate after 42 m (solid circle
 514 in C–E). Depending on the injection location (C) next to the structure S3 or (D) S1, the near
 515 field was more likely along the natural, pre-existing fractures, and it formed an ellipsoidal
 516 extension. (E) The pore pressure observations outside of the cylinder agreed often with the
 517 deviatoric component. Even in the cylinder, negative pore pressure was observed due to the
 518 deviatoric stress field and undrained dominant fault response, which acted in concert.

519

520
521522 **Table 1.** Parameters of the poroelastic model used for the poroelastic solution.

Quantity	Value	Unit
p_0	7812	[kPa] (<i>this study</i>)
S_0	4000	[kPa] (Dutler et al., 2020)
ν	0.2	[] (Dambly et al., 2019)
ν_u	0.33	[] (Wang, 2000)
α	0.68	[] (Selvadurai, Selvaduray & Nejati, 2019)
D	0.1	[m ² /s] (<i>this study</i>)
B	0.719	[] (<i>this study</i>)
K	19	[GPa] (Dambly et al., 2019)
G	10	[GPa] (Dambly et al., 2019)

523
524